Accepted Manuscript

Crack Propagation and Microwave Healing of Ferrite-filled Asphalt

Mixes Based on Image Correlation Observations

Xingyi Zhu[1], Yinhong Fan[1], Ying Yu[2, 4*] , Francisco A. Gilabert [3]

[1]Key Laboratory of Road and Traffic Engineering of Ministry of Education, Tongji University,
Shanghai 200092, P. R. China

[2] Department of Civil Engineering, Shantou University, Shantou 515063, P. R. China

[3] Ghent University, Mechanics of Materials and Structures, Tech Lane Ghent Science Park –
Campus A, Technologiepark-Zwijnaarde 46, Zwijnaarde, 9052 Ghent, Belgium

[4]Jiangsu Province Key Laboratory of Structure Engineering, Suzhou 215011, China

Abstract

One of the most important features of asphalt mixes is their ability to undergo self-healing after certain time intervals. Increasing the temperature can accelerate the healing process. In this study, the heating process will be triggered by using microwave technology when ferrite powders is added in asphalt mixes. Fracture tests were performed on open-graded friction course (OGFC) asphalt and ferrite-filled asphalt mixes under three-point bending with different heating and resting time periods. To examine the improvements in the microwave healing and fracture response of ferrite-filled asphalt mixes, the fracture process zone (FPZ) was characterized and quantified through digital image correlation. The FPZ lengths of the specimen with and without ferrite powder were compared. The asphalt specimens including ferrite powders are proved to have a relative longer FPZ length providing an improved cohesive response and a higher cracking resistance.

Key words:

microwave healing; crack propagation; ferrite powders; digital image correlation; fracture process zone

1. Introduction

Open-graded porous asphalt mixes have been increasingly used as surfacing pavement materials in order to efficiently improve the safety characteristics of road networks and to reduce noise [1]. However, due to the open nature of these materials, the asphalt binder, which is the binding system between the aggregate particles, oxidizes and ages rapidly, and thus material stiffening and embrittlement occur [2]. Raveling, which refers to the loss of particles from the top pavement surface, is the main drawback of an in-service porous asphalt [3]. Therefore, various maintenance technologies have been developed the previous years in order to prevent the aging of porous asphalt pavements. One technology involves triggering the self-healing ability of asphaltic materials through electromagnetic induction or microwave irradiation[4]. Particularly, self-healing is the ability of a material to repair damage caused by external force over time. Several studies of the self-healing mechanisms of asphalt mixes have been conducted. Bazin and Saunier [5] studied the healing properties of asphalt mixes. They found that the fatigued or even broken asphalt mixes can be healed to some degree after certain resting time periods and thus the concept of self-healing was

---

* Corresponding author. E-mail: yuying@stu.edu.cn

proposed. Little and Bhasin [6] stated that self-healing occurs due to the diffusion of the molecules across the two sides of a crack. This phenomenon creates connection points which may lead to the partial reconstruction of the material's continuity.

The factors influencing the self-healing behavior have attracted considerable interest. Temperature is considered as the main factor affecting self-healing behavior. Grant [7] found that the healing rate can be increased at high temperature by shortening the heating time periods. Daniel and Kim [8] found that the amount of stiffness gain seemed to increase when specimens were subjected to a higher temperature during the resting periods. Certain types of asphalt behaves similarly to a Newtonian fluids between 30 and 70 ℃ [9]. These types of asphalt start to flow and heal the microcracks.

The temperature-dependent characteristics of healing offers a potential way to heal the asphalt mixes through asphalt flow and diffusion at a high temperature. To accomplish this, various technologies have been proposed to trigger the self-healing ability of asphaltic materials. Chiostri et al. [10] established the microwave heating model and found that microwaves can cause a rapid heating through radiant heat transfer. Therefore, microwave heating is therefore used to trigger the healing of asphalt mixes. This is called the microwave healing. Microwave heating can also provide an uniform heating without overheating the surface of the asphalt mixes [11]. It also allows deep heating without a large difference in the temperature of the surface and the bottom of the asphalt pavements [12]. Microwave heating has advantages over conventional heating [13] and can be applied in the field of pavement recycling [14] and asphalt pavement production [15]. However, microwave heating also has certain drawbacks.

The efficiency of asphalt absorbing microwave energy depends on its dielectric properties[12]. Asphalt has poor dielectric properties at microwave frequencies [16]. Qiu [17] stated that only some magnetite-bearing aggregates and mineral powders in asphalt concrete can absorb electromagnetic waves. Therefore, the heating efficiency of asphalt concrete should be enhanced. However, the microcracks in asphalt cannot heal efficiently because the asphalt mastic lacks the ability to absorb the microwaves [18, 19]. Apostolidis et al. [20] found that adding iron powders and steel fibers to asphalt mortar could increase its electrical conductivity and magnetic permeability of asphalt thus enhancing the capacity of the material to absorb electromagnetic waves. Graphite, carbonyl iron powders and carbon nanotubes are added to asphalt to improve its microwave absorbing characteristics [16, 21]. Wu et al. [22], Liu et al. [23], and Garcia et al.[24, 25] have concluded that the optimum steel wool (a type of inductive fibers) content in asphalt mixes is between 1.5% and 5% by weight of the asphalt mixes, depending on the type of asphalt mixes and the addition of other additives, such as graphite.

Various additives significantly enhance the healing efficiency of asphalt mixes. Wang et al. [26] found that the fatigue resistance and healing capacity of the asphalt concrete containing steel fiber and graphite were higher than those of neat asphalt concrete after microwave healing. Zhu et al. [27] found that when asphalt mixes were filled with 80% ferrite powders (volume fraction of mineral powders), the fatigue life extension rate can reached 1.33 after microwave heating and 3 hours of resting time periods. According to the reference by Zhu et al.[27], under microwave irradiation, ferrite powders in asphalt mastic can absorb the microwave and convert them into heat, which increases the temperature and ultimately the microwave healing efficiency of the asphalt mastic.

Asphalt mixes are heterogeneous materials, and their fracture behavior is complicated.

83 Obtaining the fracture parameters is difficult due to the difficulties in observing the entire fracture
84 process directly. To obtain more experimental data, a full-field measurement method is required. In
85 the last decade, the use of full-field non-contact optical measurement techniques has become
86 increasingly popular for investigating fracture behavior [28]. Several experimental techniques such
87 as acoustic emission [29-31], scanning electron microscopy (SEM) [32, 33] and laser-speckle
88 interferometry [34, 35] have been used to investigate the fracture process zone (FPZ). A relatively
89 new technique called digital image correlation (DIC) is becoming popular for investigating the
90 healing behavior of asphalt mixes. Kim and Wen[36] were the first to use DIC to measure
91 displacements and strains in asphalt mixes. DIC is an optical technique used to visualize and
92 quantify the relative displacements of a set of points (speckle pattern) marked on a specimen's
93 surface. The displacements of the marked points can be tracked by comparing the digital images of
94 a specimen's surface between successive steps during the loading process, the displacements of
95 painted points can be tracked. This field of displacement allows the direct derivation of the strain
96 field. DIC is especially suitable for detecting, locating and tracking cracks, which are seeing like a
97 discontinuity (or jumps) in the displacement field. In rock-concrete interfaces, DIC has been
98 successfully applied to three-point bending (TPB) and four-point shearing (FPS) setups [37] in rock-
99 concrete interfaces to understand the crack propagation and to assess the size of the FPZ. Due to its
100 high responsiveness, high accuracy and non-destructive nature of the DIC technique, it is also used
101 to investigate the cracking behavior of the hot mix asphalt (HMA), including the fracture and fatigue
102 behavior of asphalt mixes[38]

103 The aim of this study was to investigate the microwave healing behaviors of traditional open-
104 graded friction course (OGFC) and ferrite-filled asphalt mixes. Four types of asphalt mixes were
105 considered: asphalt mixes with and without ferrite powders in their first fracture process and asphalt
106 mixes with and without ferrite powders after recovery. Two different tests were conducted on the
107 mixes: the displacement-controlled mode semi-circular bending (SCB) test and stress-controlled
108 mode SCB test. The damage process of specimens was investigated and the fracture event was
109 recorded with cameras to enable DIC measurements. The microwave healing behavior was
110 characterized by quantifying and comparing their fracture properties of the four asphalt mixes
111 according to DIC observations.

112

2. Material preparation

114 The mix proportion of the asphalt mixes was designed according to the OGFC-13 gradation
115 presented in Table 1. The asphalt–aggregate ratio was 4.7%. A total of 20 specimens of two types
116 of OGFC mixtures (with and without ferrite powders) were prepared for the conducted tests. The
117 aggregate used in the test was limestone. The properties of OGFC-13 asphalt mixes are presented
118 in Table 2.

119

120   Table 1 Gradation of OGFC-13 asphalt mixes.

Sieve size/mm	13.2	9.5	4.75	2.36	1.18	0.6	0.3	0.15	0.075
Passing rate/%	93.8	75.6	27.7	19.3	16.2	12.2	9.2	7.5	6.0

121

122

Table 2 Marshall test results of OGFC-13 asphalt mixes.

Properties	Bulk specific gravity	VV/%	VMA/%	VFA/%	Marshall stability /KN	Flow value/mm
Value	2.126	19.85	29.51	32.74	5.12	3.084

123

124   The ferrite powder used in asphalt mixes was Mn-Zn ferrite powder of high initial permeability
125 and residual magnetization. This ferrite powder can absorb microwaves and transform them into
126 heat energy [39]. In this study, the equivalent volume replacement method was adopted. In this
127 method, a certain volume of mineral fillers in a mixture is replaced by the same volume of ferrite
128 powders. The mass of mineral fillers is converted into a particular mass of ferrite powders according
129 to the following equation:

$$m_{fe} = \frac{m_k \times \rho_{fe}}{\rho_k} \tag{1}$$

130 where m_{fe} is the mass of ferrite powders, m_k is the mass of mineral fillers, ρ_{fe} is the apparent
131 density of ferrite powders (4.464 g·cm^{-3}) and ρ_{fe} is the apparent density of mineral fillers (2.740
132 g·cm^{-3}).

133   Zhu et al. [40] investigated the pavement performance, mechanical properties, and heating
134 efficiency of asphalt mixes with different ferrite concentrations. Mixtures with 5% ferrite powders
135 exhibited the best performance. According to Eq. (1), the mass ratio of ferrite powders to mineral
136 fillers in this study was 5.365:1.

3.   Experimental methods

137

138   The approach proposed in this paper for analyzing the healing process of porous asphalt mixes
139 comprises four basic steps: (i) create a controlled amount of damage in the specimens through two
140 types of mechanical testing, (ii) heat the specimens through microwave irradiation, (iii) repeat the
141 mechanical testing conducted in step (i) to check whether the damage has healed, and (iv) assess
142 the differences between mixtures with and without ferrite by using DIC.

143 **3.1 SCB test**

144   The SCB test was originally developed to measure the cracking susceptibility of asphalt [41].
145 In this test, a diametrically halved cylinder is loaded in a TPB setup. A notch (starter crack) is sawn
146 to promote the initiation and crack propagation. The SCB setup offers some advantages. The
147 geometry of the specimen is straightforward, and the specimen is easy to prepare. Moreover, the
148 specimen has a sufficiently large area for DIC technology. The specimen geometry and load
149 configuration enable the achievement of controlled crack growth, which is easy to monitor. Due to
150 the aforementioned factors, the SCB setup is suitable for testing asphalt mixes.

151   A universal testing machine (Servo-Hydraulic Universal Testing Machine UTM, 30 kN cap,
152 79-PV70B02) equipped with a temperature control chamber was used for the SCB test. Fatigue
153 testing is generally recommended at four temperatures: 10°C, 15°C, 20°C, and 25°C. Most of the
154 expected in situ damage occurs within the aforementioned temperatures [42]. To avoid an excessive
155 number of variables, the SCB test was conducted at 15°C, which is considered as an intermediate
156 temperature. As displayed in Fig. 1, the setup for the SCB test comprised two supporting rollers at
157 the bottom edge and a loading roller at the middle point of the top edge. The distance between
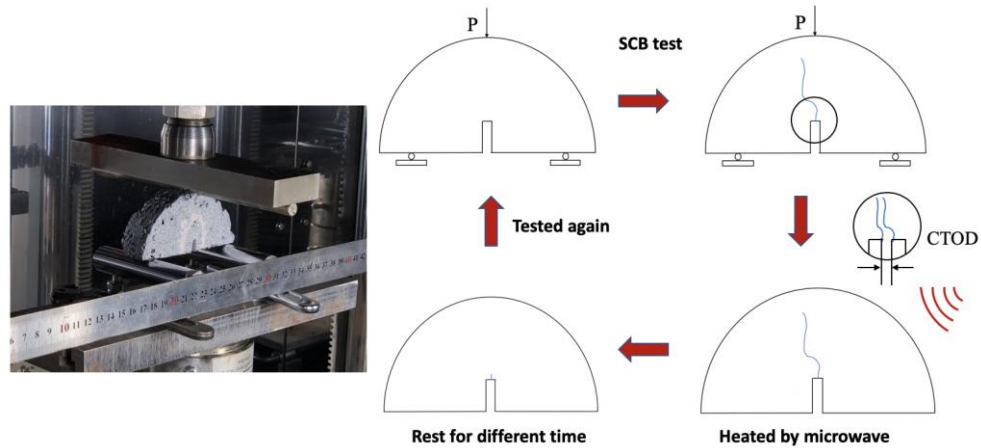158 supporters was 80 mm, which was four to five times the diameter.

Fig. 1. Process of the SCB test.

3.2 Specimen preparation

The Superpave gyratory compactor was used to compact cylinder-shaped specimens of HMA. These cylinders had a diameter of 100 mm and height of 50 mm. Two shorter cylinders were obtained from each cylinder by cutting it perpendicular to the axial direction. Next, each slice was cut perpendicular to its thickness into two identical semicircular halves and an edge notch was created in the middle of the semicircular base. **Error! Reference source not found.** displays the final geometry of the SCB specimens. The final dimensions were as follows: diameter = 100 mm, depth = 25 mm, notch length = 10 mm, and notch width = 4 mm.

3.3 Loading conditions

Two loading modes were applied: the displacement- and stress-controlled modes. The displacement-controlled-mode SCB test was used to determine the fracture toughness of the asphalt mixes [43]. The aforementioned mode allows the determination load at which the specimen fails. The stress-controlled mode, in which a test specimen is loaded with a cyclic sine signal, allows the experimental evaluation of the fatigue life extension of asphalt mixes.

3.3.1 Displacement-controlled-mode SCB test

The displacement-controlled-mode SCB test was conducted according to the ASTM D8044-16 standard. A constant displacement rate of 5 mm/min was applied to the specimen until failure. As depicted in Fig. 2, the specimen remained unchanged until it split suddenly into two pieces due to a well-developed pre-cracked area along its middle. The two pieces were manually joined without applying pressure to guarantee minimum connection between both crack faces. Next, the specimen was heated in a microwave and rested at 15°C. Finally, the specimen was tested again at 15°C to obtain the corresponding crack tip opening displacement (CTOD). Table 3 presents the nomenclature of the specimens tested under different conditions and periods of heating. A traditional OGFC asphalt mix (s1) and ferrite-filled asphalt mix (s2) were selected for testing.
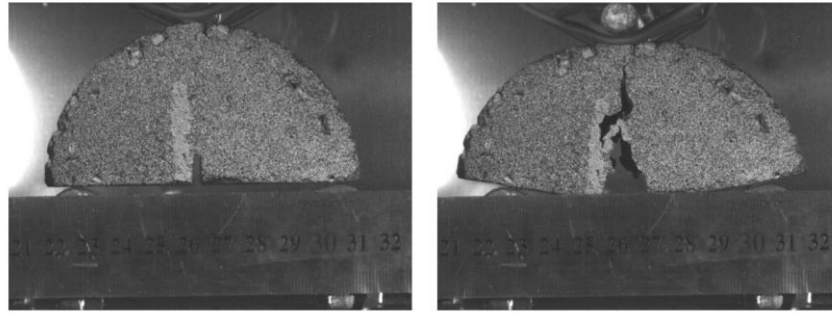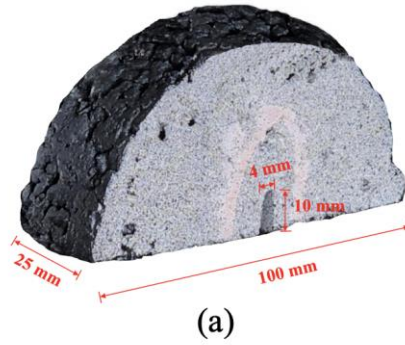
Fig. 2. (a) SCB specimen. (b) SCB specimen before testing (left) and failure of the specimen after testing (right).

Table 3 Testing conditions of different specimens in the displacement-controlled-mode SCB test.

Number	Ferrite content/%	Heating time Periods/s	Resting Time Periods/h
s1	0	0	0
s1(after recovery)	0	80	5
s2	5	0	0
s2(after recovery)	5	80	5

3.3.2 Stress-controlled-mode SCB test

The stress-controlled mode is suitable for performing fatigue tests. In the SCB fatigue tests, the stress amplitude was 0.2 kN and the stress ratio was 0.4. The frequency of the repeated compressive load was 10 Hz. This frequency consisted of a 0.1-s half-sine load and no rest period under different stress levels, which is approximately equivalent to a vehicle speed of 50 mph (approximately 80 km/h). To assess the benefits of ferrite powder in microwave heating and to quantify the effects of the resting and heating periods on the microwave healing process, the specimens were damaged until they failed. The specimens split into two pieces that looked identical to the pieces in the displacement-controlled-mode SCB test. These specimens were then heated and rested for a certain time. Finally, the specimens were damaged again by using the same fatigue loading. Table 4 presents the details of the experiments and test conditions. The first number indicates the ferrite content of the specimens. The number after the first underscore indicates the heating period of the specimen in seconds, and the number after the second underscore indicates the resting period in hours. For example, s0_40_5 represents a heating period of 40 s followed by a resting period of 5 h.

206   Table 4 Details of the different specimens used in the stress-controlled-mode SCB test.

Number	Ferrite content/%	Heating Time Periods/s	Resting Time Periods/h
s0_40_5	0	40	5
s0_40_15		40	15
s5_40_5	5	40	5
s5_40_15		40	15
s0_100_5	0	100	5
s0_100_15		100	15
s5_100_5	5	100	5
s5_100_15		100	15

3.4 Microwave heating

208   Microwave heating experiments were performed at a frequency of 2.45 GHz by using a
209   conventional microwave heating oven with a capacity of 300 W. The size of the coil of the
210   microwave heating machine was 150 mm × 500 mm. Specimens were heated in the microwave for
211   a certain period and then rested at room temperature for several hours to cool down. The details of
212   the microwave heating experiment are provided in section 3.1.

3.5 DIC implementation

214   The DIC setup displayed was used to obtain the full-field displacements and strains of the front
215   surface of the specimen. Prior to image capturing, the surface of the specimen was conveniently
216   treated to obtain a high-quality speckle pattern. The surface was first sprayed homogeneously in
217   white. Next, randomly distributed black dots were sprayed in a similar manner.

218   To capture images continuously during the experiment, a charge-coupled device (CCD) camera
219   was used to examine the two-dimensional plane deformation. A Nikon camera (SP AF17-50mm
220   F/2.8) equipped with a 50-mm macrolens with manual control of the aperture, focus, and zoom was
221   used for image capturing. The parameters of the camera are presented in Table 5. The in-plane
222   displacement resolution was 0.0000001 × the field of view (FOV). According to the parameters of
223   the camera as well as the distance between the specimen and the camera, the linear FOV was
224   calculated to be 6.9 mm/m. From the linear FOV, the displacement accuracy was calculated to be
225   0.69 µm. A subset size of 17 pixels and a step size of 1 were used for the DIC analysis. Two white
226   light sources were mounted on both sides of the specimen to achieve superior illumination and
227   image quality. The VIC-2D image processing software (Correlated Solutions Inc., USA) was used
228   to analyze the displacement/strain field of the specimen. This software enables the measurement of
229   the surface topography, displacement, and strain data for the full FOV in a two-dimensional space.
230   The specimen dimensions were measured precisely before testing, and the software calibration tool
231   was used to calibrate the scale of the reference image for each test according to the specimen
232   measurements.

233   Table 5 Parameters of the high-speed CCD camera and DIC analysis.

Frame rate (Hz)	Sensor size of camera(")	Field of view (mm/m)	In-plane displacement resolution	Displacement accuracy (μm)	DIC analysis subset (pixel)	DIC analysis step size
25	0.623	6.9	0.0000001 * FOV	0.69	17	1

7

4. Methodology: crack propagation analysis

The fracture behavior of the mixes was investigated using the cohesive zone model (CZM). The CZM is a useful for modeling crack development in asphaltic materials. It can be used to model a crack along bimaterial interfaces (such as aggregate–asphalt interfaces). This type of interface is considered a weak zone that is prone to failure. The CZM is introduced in the following text.

4.1 CZM

Barenblatt [44] proposed a cohesive model for investigating the fracture behavior of ductile and brittle materials. The cohesive crack concept was later successfully extended by Hillerborg et al. [45] to study nonlinear fracture processes. Furthermore, the CZM has been recently used to simulate the fracture process in different materials systems under various loading conditions.

Various mechanisms are active around the crack tip for the dissipation of inelastic energy, as displayed in Fig. 3 (a). CZM is a mathematical representation that describes a damaged diffuse area. This mathematical abstraction represents a single virtual crack that combines all the damage mechanisms in a diffuse area. The length of the FPZ (l_{FPZ}) is defined as the length of a virtual crack that quantifies the extension of the damaged diffuse area.

According to the fictitious crack model proposed by Hillerborg [45], stresses act across a crack as it narrowly opens. The aforementioned model is applicable only to mode I (the opening mode).

The crack is assumed to propagate when the stress at the crack tip reaches the tensile strength f_t. When the crack opens, the stress is not assumed to fall to zero at once but to decrease with an increase in width w (namely the CTOD), as displayed in Fig. 3 (b). At the stress-free crack opening displacement w_c, the stress decreases to zero. The FPZ can be defined as a region with nonzero surface traction values within the separating surfaces. Thus, the processes occurring within the process zone dissipate energy.

As displayed in Fig. 3 (b), during crack propagation, a cohesive crack zone is formed at the front end of the virtual macrocrack. This zone corresponds to the FPZ. The relationship between the length of the FPZ and the opening displacement of the crack tip is depicted in Fig. 3 (c). The FPZ begins to form when the opening displacement satisfies the condition $w > 0$. When the opening displacement fulfills the condition $w > w_c$ (w_c is the stress-free crack opening displacement), the ability to transfer stress is lost. The formula for calculating l_{FPZ} is as follows:

$$l_{FPZ} = l_{total} - l_{SFC} \tag{2}$$

where l_{SFC} is the length of the stress-free crack and l_{total} is the total length of the crack measured from the notch tip to wherever the opening displacement (w) is greater than 0.

(a)   (b)   (c)
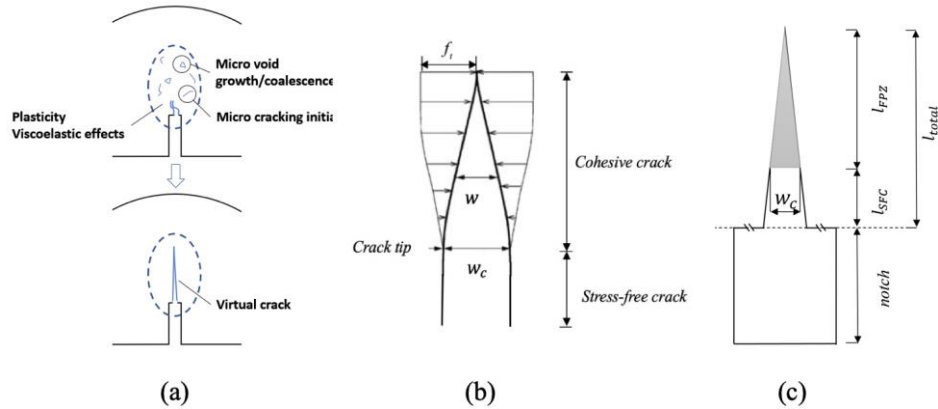
266

267   Fig. 3. (a) Virtual crack representing various mechanisms. (b) Illustration of the CZM. (c) Relationship

268   between the FPZ length and the opening displacement of the stress-free crack.

269   According to the cohesive crack concept, the cohesive stress (σ) within the FPZ can be

270 expressed as the function of the crack opening displacement (w), as illustrated in Fig. 3 (b) and (c).

271 However, the length of the FPZ depends on the value of w_c in Fig. 3 (c). Therefore, determining

272 the stress-free crack opening displacement w_c is important. Hillerborg et al. [45]and Petersson [46]

273 have proposed the bilinear softening model, which better describes the strain softening behavior of

274 concrete in the FPZ than the CZM does. In [46]], the stress-free crack opening displacement w_c

275 was $3.6G_f/f_t$ (G_f is the cohesive fracture energy and f_t is the cohesive tensile stress at crack

276 initiation). To understand the softening behavior of the rock–concrete interface, a bilinear $\sigma - w$

277 relationship was determined by Dong et al. [47], who proposed the following relationship: $w_c =$

278 $6G_f/f_t$.

279   **4.2 Calculation of the opening displacement of the stress-free crack**

280   The crack profile geometry was quantified by creating a computational grid composed of a set

281 of evenly distributed parallel lines along the vertical y-axis and perpendicular to the crack surface,

282 as displayed in Fig. 4 (a). Each line consisted of 200 pixels, where 1 pixel equaled 0.16 mm. As

283 depicted in Fig. 4 (a), line L_0 was just above the tip of the prenotch and the successive

284 lines $L_1, L_2.. L_n$ were parallel to line L_0. The distance between any two adjacent lines was 5 mm.

285 Fig. 4 (b) illustrates how the aforementioned lines were placed on a real specimen examined using

286 the DIC method. The opening displacement u along the x-axis direction and corresponding to

287 different loadings stages was derived using the DIC technique. The process is explained in the

288 following text.

(a)   (b)
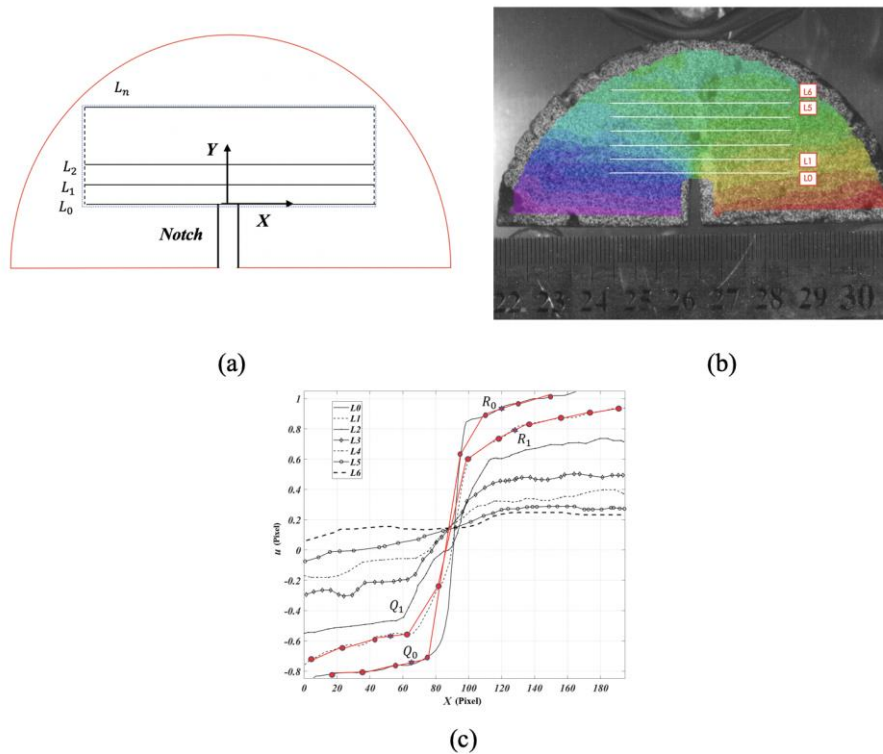

(c)

Fig. 4. (a) Schematic of the computational grid. (b) Computational grid applied on specimen s1. (c) Opening displacement calculated from the lines plotted in (b).

The displacement field at a certain time during the fracture process was used to illustrate the extraction process of the FPZ profile. Fig. 4 (c)displays the horizontal displacement along each line presented in Fig. 4 (b). Line L_0 corresponds to the notch tip and exhibits the largest jump. The opening displacement on line L_0 is obtained by directly calculating the jump of the displacement (which equals 1.6 pixels in this particular case). The jump of the displacement is determined by selecting two points at the boundaries, which are labeled as Q_0 and R_0 in Fig. 4 (c), to limit the jump. Points Q_0 and R_0 are selected as follows. Each line is divided into 3-mm intervals along its length (the interval unit must be converted from mm to pixels). The starting and ending points of the interval are connected through a line, and the slope of the line is calculated. The midpoint of an interval is selected if the slope of the previous interval is smaller than 0.01 and that of the following interval is larger than 0.01. After the difference is calculated between Q_0 and R_0 in vertical coordinates, the difference is converted from pixels to millimeters. The opening displacements on lines $L_1, L_2, ... , L_n$ are also calculated following the aforementioned procedure. The higher the line, the closer is the displacements to zero. Therefore, the crack tip can be assumed to be captured when one of the line profiles presents a horizontal line (zero jump). In this line profile, the material above the line is under a pure elastic regime. Only some small fluctuations are noted in the aforementioned profile mostly due to the heterogeneity of asphalt mixes. Caution is required when selecting points Q_0 and R_0, and the selection of these points might become highly difficult when the jump is not obvious. In this case, additional lines must be added to increase the resolution of the segmentation process. A suitable line is then selected through visual inspection. The aforementioned process is repeated for all the images were captured through DIC.

10

5. Results and discussion

5.1 General description of the damage process

This section describes the main features of the mechanical response of a displacement-controlled loaded SCB specimen under a deformation speed of 5mm/min. The magnitude of the CTOD has been taken as the main indicator of the damage process (see Fig. 1). CTOD (i.e., w) has been derived from the measurements of the opening displacement recorded via the DIC technique explained before (i.e. this is the displacement jump obtained from line L_0). Fig. 5 (a) shows a typical Force vs. CTOD curve. After a detailed observation analysis, it was deduced that the fracture process consisted of three stages. In the first stage, the material behaves mostly in a linear and elastic fashion and no visible cracks could be seen. In Fig. 5 (a), this stage corresponds to the first linear piece of the curve up to the point 1. The second stage corresponds to the piece of curve between the points 1 and 3 in Fig. 5 (a). Here, the microcracks are produced and collected in order to form a visible crack that propagates steadily. At this stage, the fracture process zone begins to form. The third stage corresponds to the curve path after point 3 in Fig. 5 (a). This last response indicated that the cracks rapidly expand producing a fast increase of the CTOD leading to a decrease of the reaction force. Fig. 5 (b) shows the crack profile and the obtained values of l_{FPZ} corresponding to the Points 1, 2 and 3 of the specimen s1. Fig. 5 (c) shows the contours of the horizontal displacement field of the specimen s1 at the points 1, 2, and 3 showed in Fig. 5 (a). This field shows that the development of the displacement around the notch is nearly anti-symmetric. The vertical cross-section at x = 0 mm can be treated as the line of anti-symmetry, where the horizontal displacement is essentially zero. As the applied load increased, a clear discontinuity or jump of the displacement field was detected. Around the notch tip, the displacement changed from -0.12mm to 0.07mm at two sides of the anti-symmetry line (x = 0 mm). The opening displacement can be interpreted as being part of a cohesive-based zone response. Since the applied load did not reach the peak, it is reasonable to assume that the displacement discontinuity can still transfer stress. In that sense, a detailed inspection of the specimen at points 2 and 3 did not reveal any visible crack or well-developed discontinuity. Therefore, despite the fact that a material connection is still visible between both sides around the displacement jump, this area can be considered as an equivalent virtual crack with both crack faces undergoing a cohesive force field. This experimental observation links well to the concept of

342 cohesive zone model (CZM) that will be treated in the next section.
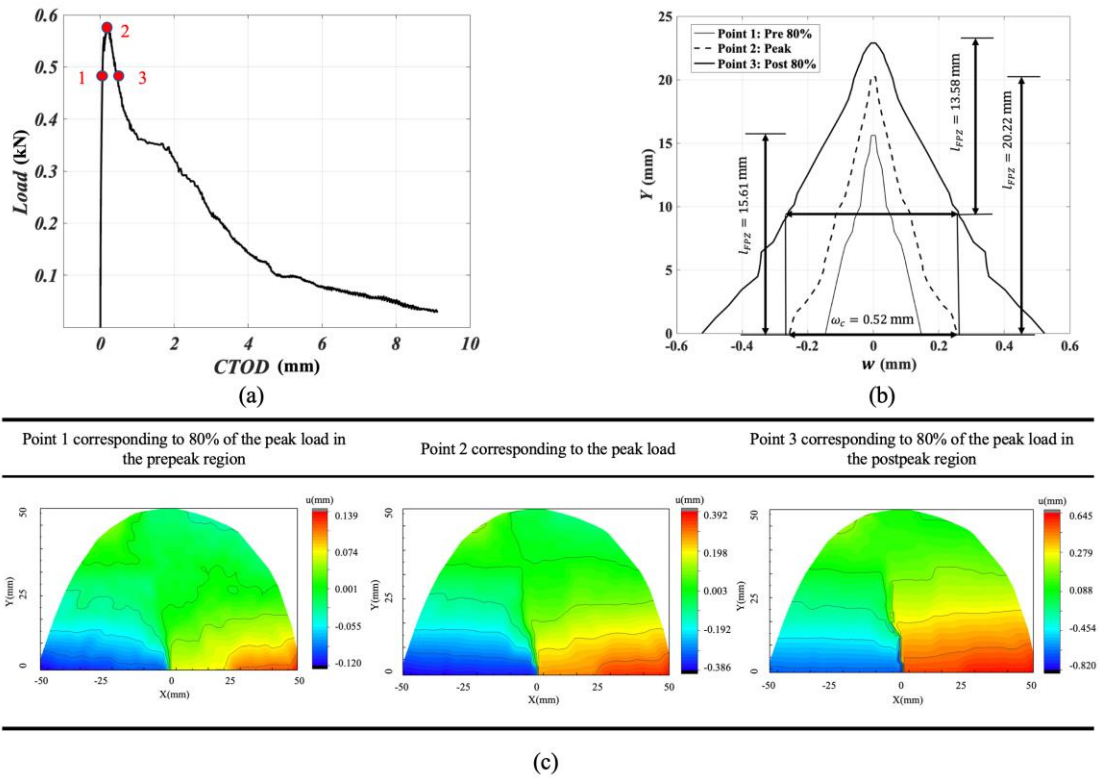
(a)

(b)

(c)

343

344 Fig. 5. (a) Damage process in the displacement-controlled mode. (b) Crack profile and l_{FPZ} of specimen s1.

345 (c) Horizontal displacement contours in displacement-controlled-mode SCB (for interpreting the color chart in this

346 figure, the reader is referred to the online version of this article).

347   With regard to the mechanical response of the SCB specimen under the stress-controlled mode,

348 Fig. 6 (a) illustrates the curve of the CTOD versus the number of cycles. Prior to the 2000th loading

349 cycle, the CTOD increased slowly. From the 2000th cycle until failure, the CTOD increased rapidly.

350 Fig. 6 (b) displays a typical force versus CTOD curve. The specimen suddenly broke apart after

351 several cycles. Fig. 6 (c)depicts the horizontal strain contours of specimen s0_40_5 at point 1 in Fig.

352 6 (a), which corresponds to 90% of the total loading period. Fig. 6 (c) also depicts the horizontal

353 displacement pattern for point 2 in Fig. 6 (a), which corresponds to 95% of the total loading period.

354 The morphologies of the aforementioned two patterns are very similar; however, the strain is higher

355 at point 2 than at point 1. Fig. 6 (d) displays the crack profiles obtained at points 1 and 2 in Fig. 6

356 (a) for specimen s0_40_5. Points 1 and 2 correspond to 90% and 95% of the total number of cycles

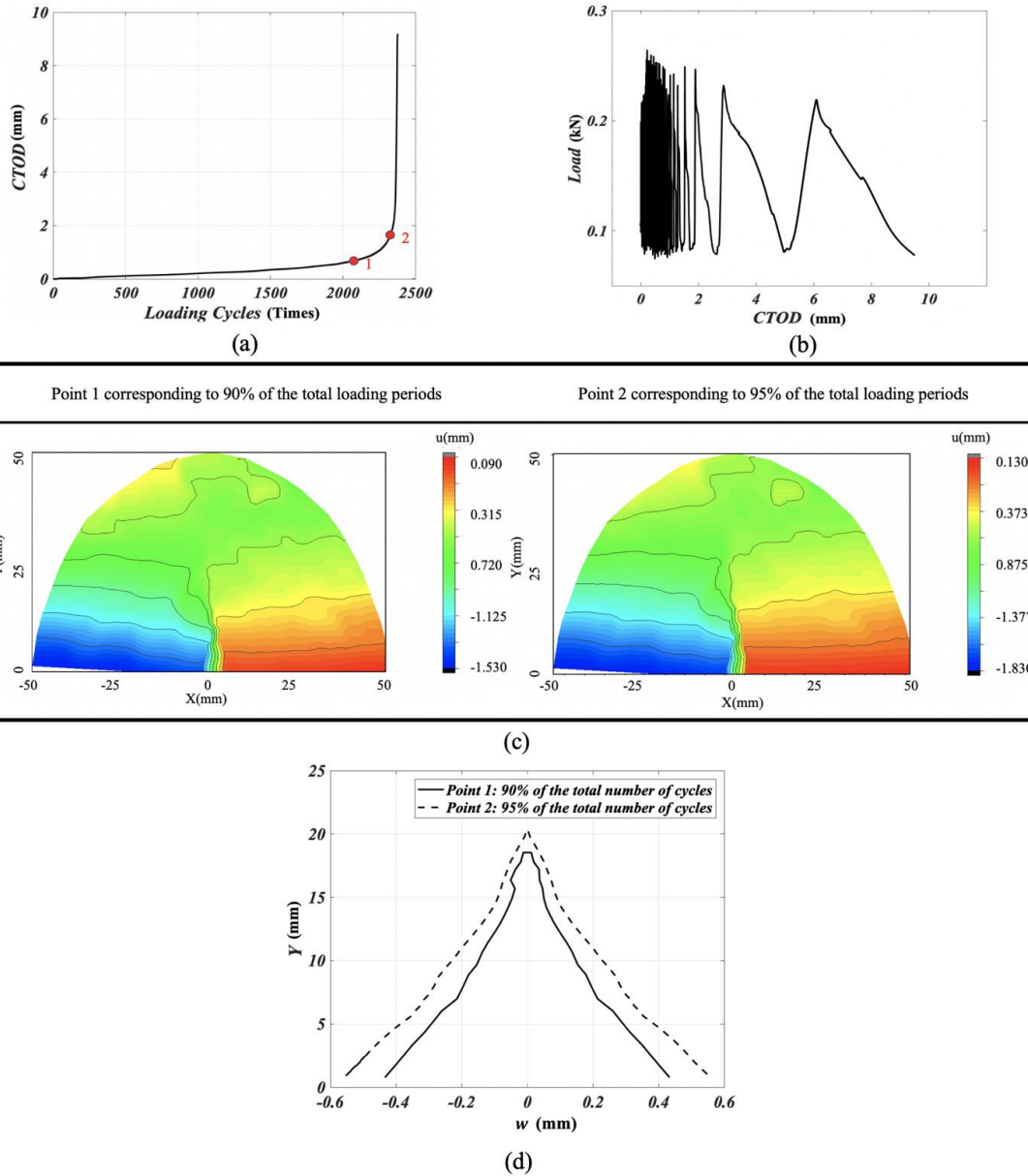357 required, respectively, for the specimen to be completely damaged.

358

Fig. 6. (a) Damage process under stress-controlled-mode SCB. (b) Damage process in the stress-controlled

process. (c) Horizontal displacement contours in the stress-controlled mode SCB (for interpretation of the color

chart in the figure, the reader is referred to the online version of this article). (d) Crack profile of specimen

s0_40_5.

5.2 Effect of the ferrite content on the FPZ

5.2.1 General response under the displacement-controlled mode

The specimen without ferrite (specimen s1) and the specimen containing ferrite (specimen s2)
were subjected to the SCB test. After being damaged, the specimens were heated in a microwave
oven for 80 s and then left to recover at room temperature for 5 h. After the resting period, the
specimens were retested to determine if any strength regain occurred. Fig. 7 illustrates the
relationship between the CTOD and the load for the specimens with and without ferrite.
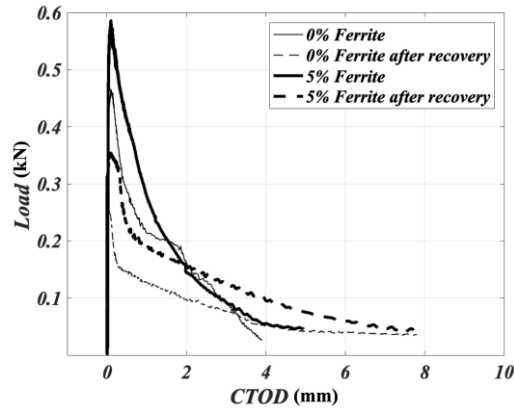
Fig. 7. Damage process for different specimen types.

Prior to the healing process, the specimen containing ferrite could withstand a larger load than the specimen without ferrite. Similarly, after the healing process, the specimen containing ferrite could better resist the effect of the load than the specimen without ferrite could. Moreover, the area under the curve was larger for the specimen containing ferrite than for the specimen without ferrite, which indicated that the addition of ferrite increased the toughness of the specimen material. Lin determined the opening displacement corresponding to the peak load as the critical opening displacement in the displacement-controlled-mode SCB test [48]. Table 6 presents the critical crack tip opening displacement of the displacement-controlled-mode SCB test. At the moment of the peak load, all the specimens had similar crack tip opening displacements.

Table 6 Critical opening displacement of the specimens at peak load.

Specimen's type	CTOD (mm)
0% Ferrite	0.51
0% Ferrite after recover	0.47
5% Ferrite	0.5
5% Ferrite after recover	0.45

The energy required to damage specimens is obtained according to the following formula:

$$W = \int_{0}^{\delta} P \, dw \qquad (3)$$

where P is the load applied to the specimen, dw is the infinitesimal increment of the CTOD, and δ is the maximum CTOD measured in the test.

The energy required to damage different types of specimens according to Eq. (3) is presented in Table 7. The energy required to damage the ferrite-filled specimens obtained before recovery and after healing is greater than that required to damage the specimen without ferrite. This result indicates that adding ferrite to asphalt mixes increases the toughness of the material. A plausible reason for this finding is that rounded ferrite particles enhance the wrapping process with asphalt. Therefore, the mastic generated by the ferrite and limestone filler has a good covering and wrapping

14

393   of aggregates in the mixture [49].

394   Table 7 Energy required for damaging different types of specimens.

Specimen / Energy (J)	s1	s1 (after recovery)	s2	s2 (after recovery)
Corresponding to pre 80%	0.060	0.050	0.059	0.061
Corresponding to peak	0.184	0.092	0.211	0.122
Corresponding to post 80%	0.453	0.135	0.427	0.360
Whole process	0.685	0.576	0.856	0.919

395

396   Fig. 8 illustrates the final state of the specimen after recovery, where a virtual crack idealized

397   by the concept of the CZM is well developed in the sample. Because the length of the FPZ was

398   calculated in all cases, the energy release rate (G) could be calculated for specimens s1 and s2 before

399   and after recovery. The parameter G represents the energy per unit surface required to create a virtual

400   crack of length l_{FPZ} (Fig. 8). This parameter (unit: J/m^2) is calculated as follows: $G =$

401    $W/(l_{FPZ} \cdot depth)$. Table 8 presents the results obtained for specimens s1 and s2.

402   The energy release rate of the ferrite-filled specimen (s2) before recovery was smaller than that

403   of the specimen without ferrite (s1). However, the energy release rate of the ferrite-filled specimen

404   after recovery was significantly larger than that of the specimen without ferrite. This result indicates

405   that the addition of ferrite improves the microwave healing behavior. Damage mechanisms, such as

406   microvoids and microcracks, were better cured after microwave heating. Thus, the microwave

407   healing behavior and energy release rate of the ferrite-filled specimen were superior to those of the

408   specimen without ferrite.
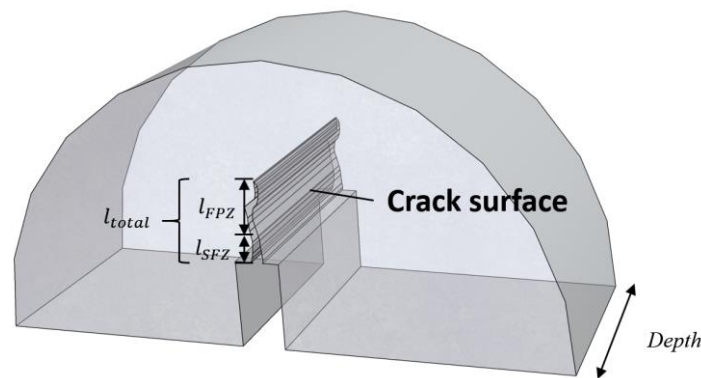
409

410   Fig. 8. Schematic of a CZM-based virtual crack in which the FPZ length is indicated.

411   Table 8 Energy release rates of different specimen types.

Specimen / G (J/m^2)	s1	s1 (after recovery)	s2	s2 (after recovery)
Corresponding to pre 80%	163.1	172.4	152.5	166.5
Corresponding to peak	436.8	252.2	417.7	290.7
Corresponding to post 80%	1518.8	509.9	1258.7	1068.8

412

413

5.2.2 FPZ and dissipated energy in displacement-controlled-mode SCB

Fig. 9 displays the evolution of l_{FPZ} for specimens with and without ferrite under displacement-controlled-mode SCB. The *x*-axis indicates the proportion of the applied load with respect to the peak load. In Fig. 23, "pre" represents that the specimen is going through the fracture process before the peak load and "post" represents the process after the peak load. According to the aforementioned figure, all the studied cases exhibited the same global trend. As the load increased, l_{FPZ} increased continuously; however, when the load decreased, l_{FPZ} decreased rapidly. At the pre70–post80 stage, the specimen with ferrite had the highest l_{FPZ} value before healing; however, after healing, l_{FPZ} was similar to the values obtained for the specimens without ferrite before healing. The specimen without ferrite had the smallest l_{FPZ} value after healing. A longer FPZ length indicates a larger damaged region with more energy dissipation. A longer FPZ might also indicate a larger area of the active plastic zone [50]. Therefore, the addition of ferrite to asphalt mixes leads to a noticeable increase in energy dissipation, which leads to superior resistance for crack propagation.
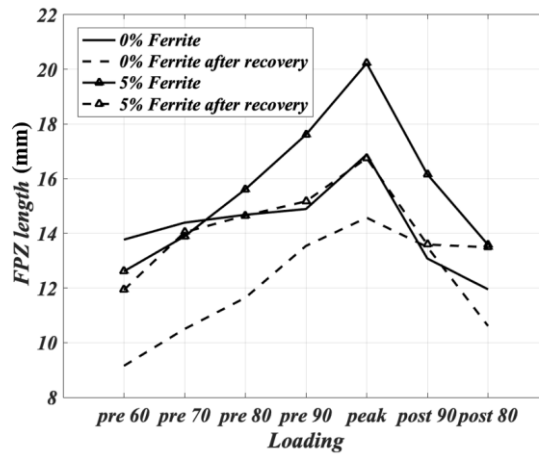

Fig. 9. FPZ lengths for different types of specimens.

The relationship between l_{FPZ} and the absorbed energy is plotted in Fig. 10. A well-developed FPZ has a large area in which the tensile and shear cohesive forces increase dissipation during fracture propagation. The FPZ length was typically longer for the specimens with ferrite powders than for those without ferrite. The energy required to damage the ferrite-filled specimens obtained before recovery and after healing was greater than that required for damaging the specimen without ferrite. This result suggests that the addition of ferrite powders to asphalt mixes increases the overall material toughness without negatively altering the microwave healing capability of the mixes.
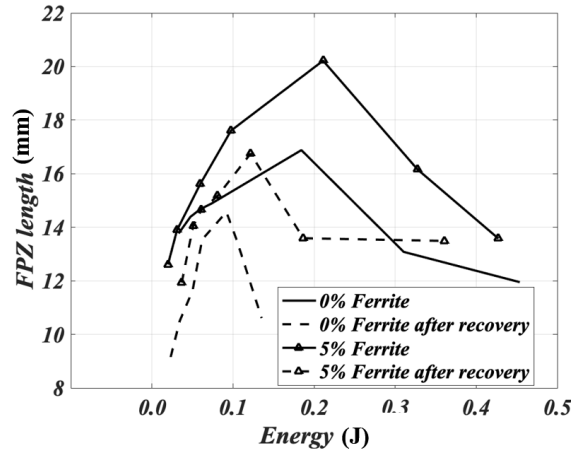
440

441   Fig. 10. Relationship between the FPZ length and energy under displacement-controlled-mode SCB.

442

5.2.3 Determination of #stress-free crack opening displacement in the stress-controlled mode

445   The stress-free crack opening displacements under displacement-controlled-mode SCB are
446   presented in Table 6. To understand the influence of w_c in the stress-controlled-mode SCB test,
447   sensitivity analysis was performed by considering the following values of w_c: 0.4, 0.5, 0.6, and 0.7
448   mm. The method for determining the most suitable value for the asphalt mixes is discussed in the
449   following section. In this regard, the variation of l_{FPZ} at different loading stages during the damage
450   process was analyzed within the proposed range of w_c.
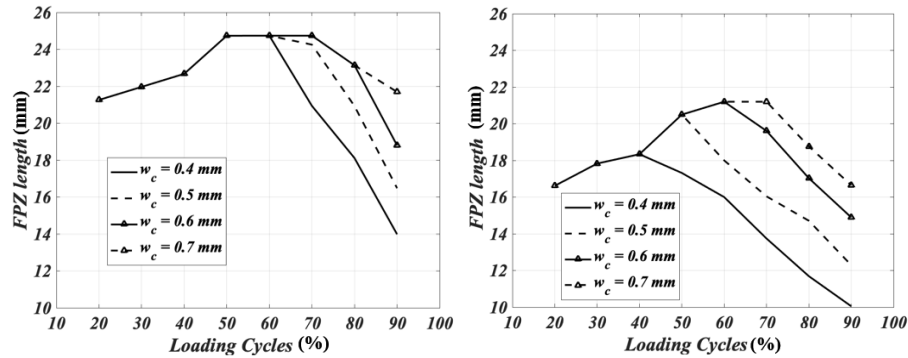
451

452

453   Fig. 11. FPZ length of specimen s5_100_5 with ferrite: (left) before recovery and (right) after recovery.

454   Fig. 11 illustrates the evolution in l_{FPZ} with the number of cycles for specimen s5_100_5 with
455   ferrite before and after recovery. The horizontal coordinate indicates the percentage of the total
456   number of cycles required for the specimen to be completely damaged. The left part of Fig. 11
457   indicates that the l_{FPZ} value of the specimen with ferrite increased with the loading cycles from a
458   loading percentage of 20% to 50% and decreased with the loading cycle beyond a loading
459   percentage of 60%. Beyond a loading percentage of 60%, l_{FPZ} changed as a function of w_c. The
460   larger the value of w_c, the higher was the energy stored in the specimen and the longer was the FPZ.
461   The smaller the value of w_c, the shorter was the value of l_{FPZ}. When the damage process reached
462   90%, l_{FPZ} was 13.98 mm for a w_c value of 0.4 mm and 21.69 mm for a w_c value of 0.7 mm. In
463   the studied range of w_c, the length of FPZ differed by up to 7.71 mm. The right part of Fig. 11

17

presents the l_{FPZ} values for different values of w_c for the same specimen after recovery. Compared with the l_{FPZ} value before healing, the l_{FPZ} reduced in each stage after healing. When the load reached 50% of total loading cycles, the length of the FPZ was 20.5 mm after healing. The corresponding length before healing was 24.74 mm. The damage in the specimen that could not be healed resulted in a smaller FPZ after recovery than that obtained before recovery. Moreover, the moment at which l_{FPZ} reached a maximum value was gradually delayed when w_c increased.
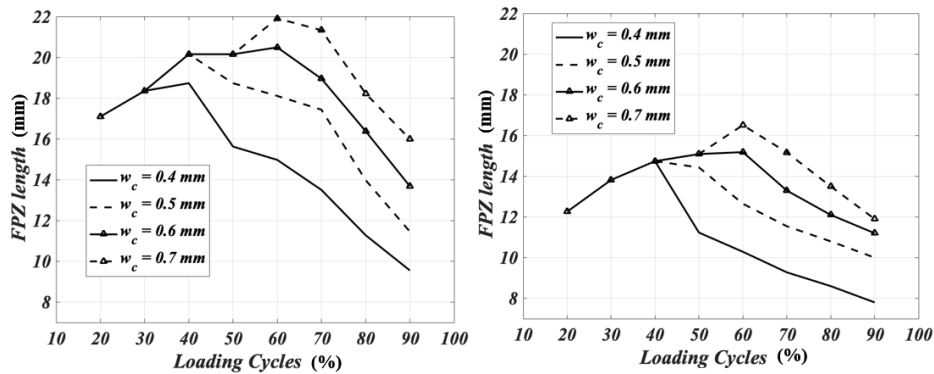
Fig. 12. FPZ length of the specimen without ferrite: (left) before healing and (right) after healing.

The left part of Fig. 12 presents the FPZ length of the specimen without ferrite (s0_100_5) before healing at different stages of the damage process. The effects of different w_c values on the FPZ were noticeable from the beginning of the damage process. In other words, compared with the previous case, the addition of ferrite increased the sensitivity of w_c. At all the damage stages, the value of l_{FPZ} was smaller for the specimen without ferrite than for the specimen with ferrite, which indicated that the crack tip opening displacement of samples with ferrite was generally larger than that of the samples without ferrite. Furthermore, the incorporation of ferrite led to decreased l_{FPZ} values. This result is in agreement with the fact that the ferrite-filled specimen had a higher toughness value than the specimen without ferrite even before the healing process. The right part of Fig. 12 presents the FPZ lengths of asphalt mixes without ferrite after healing following different damage processes. In general, the asphalt mixes without ferrite had the smallest FPZ length for all the w_c values, which indicated that these mixes had the worst capability to dissipate energy. During the mechanical test, samples of the aforementioned mixes were damaged locally prior to the full development of the FPZ.

According to the aforementioned analysis, the FPZ length calculated by setting $w_c = 0.5$ mm represents an intermediate value. Moreover, the FPZ length for the aforementioned w_c value was similar on average to the FPZ length calculated using different w_c values. When the same value of w_c was used for the specimens with and without ferrite, the differences in the fracture properties of the two types of specimens could be compared easily. Therefore, 0.5 mm was assumed to be the most reasonable w_c value for the asphalt mixes studied in this research.

5.2.4 FPZ and dissipated energy under stress-controlled mode SCB

Fig. 13 presents the FPZ length before and after the healing of specimens s0_100_5 and s5_100_5 when assuming $w_c = 0.5$ mm. This result suggests that the specimen with ferrite had the highest FPZ length before healing during the entire fracture process, whereas the ferrite-free

497 specimen had the smallest FPZ length after the healing process.
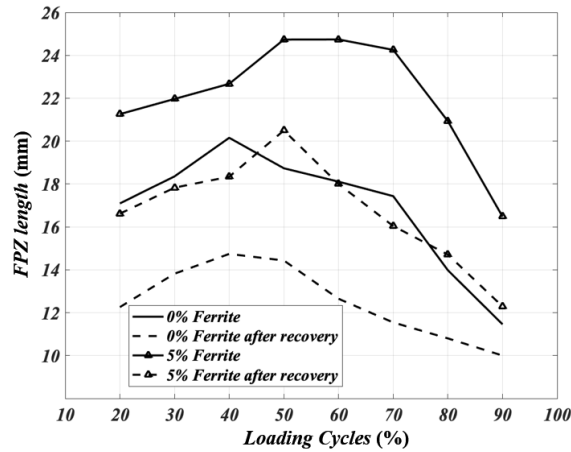
Fig. 13. Variation trend in the FPZ length under stress-controlled-mode SCB.

500   The energy required to break specimens s5_100_5 and s0_100_5 completely was obtained
501 according to Eq. (3) (Table 9). Compared with the displacement-controlled-mode SCB test, the
502 energy required for the fatigue test was significantly lower. This finding is consistent with the fact
503 that the largest energy value was required to damage the control specimens with ferrite before
504 heating, whereas the smallest energy value was required to damage the ferrite-free specimen after
505 the healing process.

506   Table 9 Energy required for damaging different types of specimens.

Specimen / Energy (J)	s5_100_5	s5_100_5 (after recovery)	s0_100_5	s0_100_5 (after recovery)
Corresponding to 60%	0.073	0.013	0.013	0.010
Corresponding to 80%	0.102	0.060	0.055	0.028
Whole process	0.160	0.123	0.107	0.087

508   The energy release rate under stress-controlled mode SCB was calculated as described in
509 Section 5.2.1, and the results are presented in Table 10. The energy release rate of the ferrite-filled
510 specimen before recovery was larger than that of the specimen without ferrite. The addition of ferrite
511 increased the toughness of the asphalt mixes before recovery. As in the previous case, the recovery
512 of G was larger for the ferrite-filled specimen than for the specimen without ferrite. Ferrite powder
513 absorbed a large amount of heat and uniformly warmed the asphalt mortar around it, which led to
514 enhanced recovery from the damage.

515   Table 10 Energy release rates of different specimen types.

Specimen / G (J/m^2)	s5_100_5	s5_100_5 (after recovery)	s0_100_5	s0_100_5 (after recovery)
Corresponding to 60%	120.4	33.6	28.7	34.7
Corresponding to 80%	191.1	164.4	157.4	103.9

5.3 Influence of the heating and resting times on the FPZ length

The influence of different heating and different healing times on the energy release rate in the fatigue test was investigated for $w_c = 0.5$ mm. The energy release rate corresponding to 80% of the fracture loading was selected to understand the process. The energy release rates for different situations in the fatigue test are summarized in Table 11.

Table 11 Energy release rate for different situations in the fatigue test.

Specimen $\qquad$ G (J/m^2)	Corresponding to 80%
s0_40_5	140.8
s5_40_5 (after recovery)	67.6
s0_40_5	215.4
s5_40_5 (after recovery)	127.4
s0_40_15	164.5
s0_40_15 (after recovery)	90.5
s5_40_15	203.6
s5_40_15 (after recovery)	146.6
s0_100_5	157.4
s0_100_5 (after recovery)	103.9
s5_100_5	191.1
s5_100_5(after recovery)	164.4
s0_100_15	171.9
s0_100_15 (after recovery)	122.0
s5_100_15	202.0
s5_100_15(after recovery)	187.9

In general, the energy release rates after recovery increased with increases in the heating and resting times. To obtain an intuitive understanding of the difference between the energy release rates before recovery and after recovery, a new index called the recovery indicator (RI) was adopted. The RI was calculated as follows:

$$\text{RI} = \frac{\text{Energy release rate}_{before\ recovery}}{\text{Energy release rate}_{after\ recovery}} \qquad (4)$$

The influence of different resting times on the specimens with and without ferrite was investigated.

Table 12 indicates that the RI increased as the resting time increased irrespective of whether the specimen contained ferrite. This result indicates that an increase in the resting time enhances the microwave healing behavior of specimens. Moreover, an increased resting time causes a greater enhancement in the microwave healing behavior of ferrite-filled specimens than in microwave healing behavior of specimens without ferrite.

537

Table 12 RI values for different resting times.

Number	Ferrite Content/%	Heating Time Periods/s	Resting Time Periods/h	RI
s0_40_5	0	40	5	0.48
s0_40_15		40	15	0.55
s5_40_5	5	40	5	0.59
s5_40_15		40	15	0.72

538

539   The influence of different heating times on specimens with and without ferrite were also
540 investigated. As presented in Table 13, the RI increased with heating time, which indicates that an
541 increased heating time enhances the microwave healing behavior of asphalt mixes. An increased
542 heating time had a larger effect on the RI than an increased resting time did. This result suggests
543 that the heating time is the most important factor affecting the microwave healing behavior of
544 asphalt mixes.

545

546

Table 13 RI values for different heating times.

Number	Ferrite Content/%	Heating Time Periods /s	Resting Time Periods /h	RI
s0_40_5	0	40	5	0.48
s0_100_5		100	15	0.66
s5_40_5	5	40	5	0.59
s5_100_5		100	5	0.86

547

6. Conclusion

549   This study investigated the fracture process of asphalt mixes with and without ferrite powders.
550 The mix proportion of the asphalt mixes were designed according to the OGFC-13 gradation. A total
551 of 20 specimens were prepared from OGFC mixtures with and without ferrite powders for the
552 displacement-controlled-mode and stress-controlled-mode SCB tests. By using the DIC technique,
553 the damage process and FPZ were evaluated. The following conclusions were drawn from this study:
554   (1) In the displacement-controlled-mode SCB test, the specimen containing 5% of ferrite could
555 withstand a higher load than the specimen without ferrite. The energy required to damage the ferrite-
556 filled specimens before recovery and after healing was greater than that required to damage the
557 specimen without ferrite. This result indicates that the addition of ferrite can increase the toughness
558 and significantly improve the microwave healing behavior of asphalt mixes.
559   (2) The addition of ferrite increased the FPZ length, which indicated that the addition of ferrite
560 to asphalt enhanced the energy dissipation process and led to an increased resistance to crack

561   propagation.

562   (3) In the stress-controlled-mode SCB test, the value of w_c was set 0.5 mm for the specimens

563   with and without ferrite to compare their damage and microwave healing capabilities.

564   (4) The specimen with ferrite obtained before healing had the longest FPZ length during the

565   entire fracture process, whereas the ferrite-free specimen obtained after the healing process had the

566   smallest FPZ length. The energy release rate of the ferrite-filled specimen before recovery was larger

567   than that of the specimen without ferrite.

568   (5) Increased resting and heating times improved the microwave healing capacity of asphalt

569   mixes. The improvement in the microwave healing capacity was strengthened with the addition of

570   ferrite powders.

571   (6) In conclusion, asphalt mixes with ferrite have a superior capacity to mixes without ferrite

572   for resisting crack propagation under fatigue loading. The addition of ferrite increases the contact

573   between aggregates and asphalt, which improves the cohesive tension effect between crack faces at

574   relatively long lengths.

575   A microlevel study should be conducted in the future to confirm the reasons for the

576   improvement in the crack resistance of asphalt mixes after the addition of ferrite to them.

577

Acknowledgements

582

References

584   [1]   Yamaguchi M, Nakagawa H, Mizuno T. Sound absorption mechanism of porous asphalt

585   pavement [J]. Journal of the Acoustical Society of Japan (E). 1999,20(1): p. 29-43.

586   [2]   Petersen JC, Harnsberger PM. Asphalt aging: dual oxidation mechanism and its

587   interrelationships with asphalt composition and oxidative age hardening [J]. Transportation Research

588   Record. 1998,1638(1): p. 47-55.

589   [3]   Mo L, Huurman M, Wu S, Molenaar A. Ravelling investigation of porous asphalt concrete

590   based on fatigue characteristics of bitumen–stone adhesion and mortar [J]. Materials & Design.

591   2009,30(1): p. 170-9.

592   [4]   Li C, Wu S, Chen Z, Tao G, Xiao Y. Enhanced heat release and self-healing properties of steel

593   slag filler based asphalt materials under microwave irradiation [J]. Construction and building materials.

594   2018,193: p. 32-41.

595   [5]   Bazin P, Saunier J, editors. Deformability, fatigue and healing properties of asphalt mixes. Intl

596   Conf Struct Design Asphalt Pvmts; 1967.

597   [6]   Little DN, Bhasin A. Exploring Mechanism of Healing in Asphalt Mixtures and Quantifying

598   its Impact. Self healing materials: Springer; 2007. p. 205-18.

599   [7]   Grant TP. Determination of asphalt mixture healing rate using the Superpave indirect tensile

600   test: University of Florida USA; 2001.

601   [8]   Daniel JS, Kim YR. Laboratory evaluation of fatigue damage and healing of asphalt mixtures

602   [J]. Journal of Materials in Civil Engineering. 2001,13(6): p. 434-40.

603   [9]   Biro S, Gandhi T, Amirkhanian S. Determination of zero shear viscosity of warm asphalt

604   binders [J]. Construction and Building Materials. 2009,23(5): p. 2080-6.

605   [10]   Chiostri M, Ceseri P. Self-propelled operating apparatus for the regeneration pavement.

606   Google Patents; 1984.

607   [11]   Bosisio R, Spooner J, Grønger J. Asphalt road maintenance with a mobile microwave power

608   unit [J]. Journal of Microwave Power. 1974,9(4): p. 381-6.

609   [12]   Al-Ohaly AA, Terrel RL. Effect of microwave heating on adhesion and moisture damage of

610   asphalt mixtures: National Research Council, Transportation Research Board; 1988.

611   [13]   Benedetto A, Calvi A. A pilot study on microwave heating for production and recycling of

612   road pavement materials [J]. Construction and Building Materials. 2013,44: p. 351-9.

613   [14]   Eliot M. Microwave processing unit for pavement recycling and asphalt pavement production.

614   Google Patents; 2014.

615   [15]   Jeppson MR. Microwave method and apparatus for heating loose paving materials. Google

616   Patents; 1986.

617   [16]   Liu W, Miao P, Wang S-Y. Increasing microwave heating efficiency of asphalt-coated

618   aggregates mixed with modified steel slag particles [J]. Journal of Materials in Civil Engineering.

619   2017,29(10): p. 04017171.

620   [17]   Qiu J. Self healing of asphalt mixtures: towards a better understanding of the mechanism: TU

621   Delft, Delft University of Technology; 2012.

622   [18]   Zhao H, Zhong S, Zhu X, Chen HJJoMiCE. High-efficiency heating characteristics of ferrite-

623   filled asphalt-based composites under microwave irradiation [J]. 2017,29(6): p. 04017007.

624   [19]   Williams D, Little D, Lytton R, Kim Y, Kim Y. Microdamage healing in asphalt and asphalt

625   concrete, volume II: Laboratory and field testing to assess and evaluate microdamage and microdamage

626   healing. 2001.

627   [20]   Apostolidis P, Liu X, Scarpas A, Kasbergen C, van de Ven M. Advanced evaluation of asphalt

628   mortar for induction healing purposes [J]. Construction and Building Materials. 2016,126: p. 9-25.

629   [21]   Miao P, Liu W, Wang SJM, Structures. Improving microwave absorption efficiency of asphalt

630   mixture by enriching Fe 3 O 4 on the surface of steel slag particles [J]. 2017,50(2): p. 134.

631   [22]   Wu S, Mo L, Shui Z, Chen Z. Investigation of the conductivity of asphalt concrete containing

632   conductive fillers [J]. Carbon. 2005,43(7): p. 1358-63.

633   [23]   Liu Q, Schlangen E, García Á, van de Ven M. Induction heating of electrically conductive

634   porous asphalt concrete [J]. Construction and Building Materials. 2010,24(7): p. 1207-13.

635   [24]   García Á, Schlangen E, van de Ven M, van Vliet D. Induction heating of mastic containing

636   conductive fibers and fillers [J]. Materials and structures. 2011,44(2): p. 499-508.

637   [25]   García Á, Schlangen E, van de Ven M, van Bochove G. Optimization of composition and

638   mixing process of a self-healing porous asphalt [J]. Construction and Building Materials. 2012,30: p. 59-

639   65.

640   [26] Wang H, Yang J, Lu G, Liu XJJoT, Evaluation. Accelerated healing in asphalt concrete via

641   laboratory microwave heating [J]. 2018,48(2): p.

642   [27] Zhu X, Cai Y, Zhong S, Zhu J, Zhao H. Self-healing efficiency of ferrite-filled asphalt mixture

643   after microwave irradiation [J]. Construction and Building Materials. 2017,141: p. 12-22.

644   [28] Romeo E. Two-dimensional digital image correlation for asphalt mixture characterisation:

645   interest and limitations [J]. Road Materials and Pavement Design. 2013,14(4): p. 747-63.

646   [29] Behnia B, Dave EV, Buttlar WG, Reis H. Characterization of embrittlement temperature of

647   asphalt materials through implementation of acoustic emission technique [J]. Construction and Building

648   Materials. 2016,111: p. 147-52.

649   [30] Sun Z, Behnia B, Buttlar W, Reis H. Assessment of low-temperature cracking in asphalt

650   materials using an acoustic emission approach [J]. Journal of Testing and Evaluation. 2017,45(6): p.

651   1948-58.

652   [31] Sun Z, Behnia B, Buttlar WG, Reis H. Acoustic emission quantitative evaluation of

653   rejuvenators to restore embrittlement temperatures to oxidized asphalt mixtures [J]. Construction and

654   Building Materials. 2016,126: p. 913-23.

655   [32] Mokhtari A, Lee HD, Williams RC, Guymon CA, Scholte JP, Schram S. A novel approach to

656   evaluate fracture surfaces of aged and rejuvenator-restored asphalt using cryo-SEM and image analysis

657   techniques [J]. Construction and Building Materials. 2017,133: p. 301-13.

658   [33] Mazumder M, Ahmed R, Ali AW, Lee S-J. SEM and ESEM techniques used for analysis of

659   asphalt binder and mixture: A state of the art review [J]. Construction and Building Materials. 2018,186:

660   p. 313-29.

661   [34] Jia Z, Shah S. Two-dimensional electronic-speckle-pattern interferometry and concrete-

662   fracture processes [J]. Experimental Mechanics. 1994,34(3): p. 262-70.

663   [35] Horii H, Ichinomiya T. Observation of fracture process zone by laser speckle technique and

664   governing mechanism in fracture of concrete. Current Trends in Concrete Fracture Research: Springer;

665   1991. p. 19-29.

666   [36] Kim YR, Wen HJAPT. Fracture energy from indirect tension testing [J]. 2002,71: p. 779-93.

667   [37] Dong W, Wu Z, Zhou X, Wang N, Kastiukas G. An experimental study on crack propagation

668   at rock-concrete interface using digital image correlation technique [J]. Engineering Fracture Mechanics.

669   2017,171: p. 50-63.

670   [38] Birgisson B, Montepara A, Romeo E, Roncella R, Roque R, Tebaldi G. An optical strain

671   measurement system for asphalt mixtures [J]. Materials and Structures. 2009,42(4): p. 427-41.

672   [39] Valenzuela R. Novel Applications of Ferrites [J]. Physics Research International,2012,(2012-

673   3-15). 2012,2012(2090-2220): p. 3202-5.

674   [40] Zhu X, Ye F, Cai Y, Birgisson B, Lee KJJoCP. Self-healing properties of ferrite-filled open-

675   graded friction course (OGFC) asphalt mixture after moisture damage [J]. 2019,232: p. 518-30.

676   [41] Krans R, Tolman F, Van de Ven M, editors. Semi-circular bending test: a practical crack growth

677   test using asphalt concrete cores. RILEM proceedings; 1996: Chapman & Hall.

678   [42] Fatigue response of asphalt-aggregate mixetures (with   discussion). Journal of the

679   Association of Asphalt Paving Technologists [J]. 1992, 61.

680   [43] Mull M, Stuart K, Yehia AJJoms. Fracture resistance characterization of chemically modified

681   crumb rubber asphalt pavement [J]. 2002,37(3): p. 557-66.

682   [44] Barenblatt GI. The mathematical theory of equilibrium cracks in brittle fracture.   Advances

683   in applied mechanics. 7: Elsevier; 1962. p. 55-129.

684   [45] Hillerborg A, Modéer M, Petersson P-E. Analysis of crack formation and crack growth in

685   concrete by means of fracture mechanics and finite elements [J]. Cement and concrete research.

686   1976,6(6): p. 773-81.

687   [46] Petersson P-E. Crack growth and development of fracture zones in plain concrete and similar

688   materials, Report No. TVBM-1006, Division of Building Materials, Lund Institute of Technology, Lund,

689   Sweden, 1981.

690   [47] Dong W, Wu Z, Zhou X. Fracture mechanisms of rock-concrete interface: experimental and

691   numerical [J]. Journal of Engineering Mechanics. 2016,142(7): p. 04016040.

692   [48] Lin Q, Yuan H, Biolzi L, Labuz JF. Opening and mixed mode fracture processes in a quasi-

693   brittle material via digital imaging [J]. Engineering Fracture Mechanics. 2014,131: p. 176-93.

694   [49] Peinado F, Medel E, Silvestre R, Garcia A. Open-grade wearing course of asphalt mixture

695   containing ferrite for use as ferromagnetic pavement [J]. Composites Part B: Engineering. 2014,57: p.

696   262-8.

697   [50] Shet C, Chandra NJJoem, technology. Analysis of energy balance when using cohesive zone

698   models to simulate fracture processes [J]. 2002,124(4): p. 440-50.

699

CRediT authorship contribution statement

Xingyi Zhu: Conceptualization, Methodology, Investigation, Writing - review & editing

Yinhong Fan: Data curation, Writing - original draft, Investigation, Software

Ying Yu: Data curation, Writing - original draft, Investigation, Software

Francisco A. Gilabert: Data curation, Writing - original draft, Investigation, Software